［共同研究成果］

Computational analysis of the body-force models for plasma actuator-assisted flow control simulations

Di Chen*: Dept. Information and Comp. Tech., Tokyo University of Science
Kengo Asada: Dept. Information and Comp. Tech., Tokyo University of Science
Satoshi Sekimoto**: Dept. Information and Comp. Tech., Tokyo University of Science
Kozo Fujii: Dept. Information and Comp. Tech., Tokyo University of Science
Hiroyuki Nishida: Tokyo University of Agriculture and Technology

* Currently, Institute of Industrial Science, University of Tokyo
** Currently, Tokyo University of Agriculture and Technology

1. Introduction

The well-known “ion wind” induced by a dielectric barrier discharge plasma actuator (DBD-PA) has been extensively used as an active flow control device to avoid flow separation thanks to the high availability and feasibility. DBD-PA only consists of two electrodes with a dielectric layer between them, see Fig. 1(a). Due to the thin and light structure, DBD-PA can be attached on any flat or curved surfaces, corner, or edge, where flow separation control[1, 2]is considered without changing the original shape of the body surface. A review conducted by Wang et al.[3] shows a number of flow control applications of DBD-PA till the year 2013. The applications include not only on separation control shown in Fig. 1(b,c)[4,5] but also on noise reduction,[6] skin-friction reduction,[7]and else.

DBD-PA for flow separation control is typically installed on the suction surface near the leading edge[1, 2] It can generate a wall-jet flows with the maximum velocity up to around 10m/s, when the peak-to-peak voltage (V_{pp}) and the base frequency of operating alternating current (AC) are 5-20kV and 1-10kHz, respectively. The ionization effect is largely determined by the applied voltage as well as electric permittivity and thickness of the dielectric layer. The mechanism of plasma-assisting flow control is described as the interaction of the ionized gas and the neutral air, which results in an electrohydrodynamic body-force field coupling with the momentum transfer in the external flow downstream of the exposed electrode.[8-11]

Massines et al.[12] and Roth et al.,[13] proposed the early model of body force field generated by a single DBD-PA, which was one-dimensional (1-D) based on static formulation and neglected the presence of the charged particles, therefore it barely fitted two-dimensional (2-D) or three-dimensional (3-D) applications. Semi-empirical models of 2-D plasma flow modelling, using linear,[14] exponential functions,[10, 11] and Gaussian distribution[2] of the spatial decay for the 2-D body force component were reviewed by Corke et al.[15] Numerous studies have made great efforts on the body-force modelling.[2, 12-14]

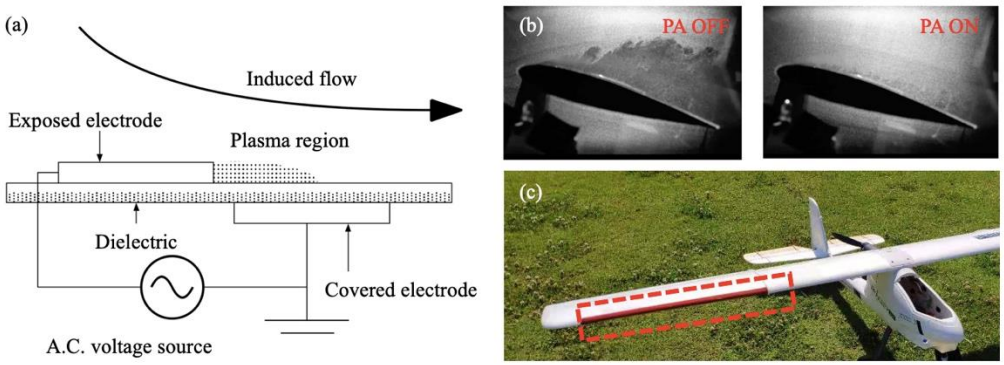

Figure 1. (a) Sketch of DBD-PA. (b) Wind tunnel test on airfoil[4]. (c) DBD-PA attached on the leading edge of a small model plane (wingspan of 3m) in a flight test[5].

The phenomenological such as Suzen-Huang (S-H) model[2] and Shyy model[14] were largely employed because of the simplicity in the computational flow simulations of Asada et al.[16,17] and Visbal et al.,[1] respectively. The well-known analytical S-H model is an electrostatic (semi-empirical) model derived from Enloe et al.'s work,[10] the body force vector can be expressed as,

$$\boldsymbol{f}_i = Q_c \boldsymbol{E}_i = Q_c(-\nabla\phi), \tag{1}$$

where $\boldsymbol{E}_i$ is the electric field vector. The force is contributed by two different parts: the external electric potential ϕ and the electric field created by the net charged density Q_c. The net body force obtained by the closed-form solution of the S-H model was well validated in the experimental study,[21] by calibrating the nondimensional plasma parameter D_c representing the scaling of the electrical to inertial forces, which also describes the strength and the scale of body force from another perspective.[16,17, 21,22] These studies indicated that the flow control authority of the plasma actuators are well realized by the simulations using these models. Airfoil stall characteristics are well simulated, and the computational and experimental pressure distributions over an airfoil agree pretty well.

Despite the low cost of using the analytical model, it is true that the S-H model neglects the complex plasma chemistry which usually causes the highly unsteady forcing on the plasma flow. On the other hand, the charged-particle models associated with the fully-coupled approaches consider the ordinary force diffusion, drift motion, Coulomb acceleration of electrons, and positive and negative ions, respectively. Drift-Diffusion (D-D) model was first developed from the physical modelling,[23-25] which focused on the electric-field effects on the charged particles. More recently the D-D model was used to simulate the discharge plasma evolution and the DBD-PA-induced body-force field.[9,26] However, due to the time-consuming computation, few studies applied the D-D model in flow control simulations. Gaitonde et al.[27] conducted plasma-based stall control simulations with coupled approaches that largely reduced the complexity of the broad-spectrum problem, nonetheless, the induced flow field of high temporal resolution during a single discharge cycle still remains unclear.

In the present study, the body-force field was obtained by the S-H model, as well as by the D-D computation of high temporal resolution. A high-fidelity Navier-Stokes solver is employed to simulate the DBD-PA induced flow with the incorporating body force field. Based on the published results by Chen et al.,[28] this report summarizes the nature of the S-H model and the D-D model, clarifies the difference between the two models from the viewpoint of the DBD-PA flow control authority, and finally provides several suggestions in using the body-force models for plasma actuator-assisted flow control simulations.

2. Methodology

2.1 Body force modelling

2.1.1 Suzen-Huang model

As we introduced in Eqn. (1), the body force vector is computed by multiplying the charge density Q_c and electric field vector $\boldsymbol{E}_i$, which are solved in the Maxwell's equations of the external electric potential ϕ and the charged particle potential, respectively, as follows

$$\nabla \cdot (\varepsilon_r \nabla \phi) = 0, \tag{2}$$

$$\nabla \cdot (\varepsilon_r \nabla Q_c) = \frac{Q_c}{\lambda_d^2}, \tag{3}$$

where ε_r denotes the relative permittivity of the dielectric layer, and λ_d denotes the Debye length. In Fig. 2(a), the boundary conditions for solving Eqn. (2) and (3) on the exposed electrode and the wall above the covered electrode can be written as

$$\phi(t) = \phi^{max} f(t), \tag{4}$$

$$Q_{c,w}(x,t) = Q_c^{max} G(x) f(t), \tag{5}$$

respectively, where ϕ^{max} and Q_c^{max} are the maximum values of the external electric potential and the charge density, respectively. Consequently, the time variation of the non-dimensional S-H body force is given as follows

$$\boldsymbol{S}_i(x,y,z,t) = D_c \sin^2(2\pi F_{base} t)\, \boldsymbol{S}_{SH}(x,y,z), \tag{6}$$

where F_{base} is the nondimensional base frequency of the AC power, $\boldsymbol{S}_{SH}$ is the non-dimensional body-force vector of S-H model. $\boldsymbol{S}_{SH}$ follows a half Gaussian function $G(x)$ in two-dimensional spatial distribution described in Fig. 2(b).[2] The magnitude of the S-H body force is manipulated by the nondimensional plasma parameter D_c, which is given empirically as

$$D_c = \frac{Q_{c,ref} E_{ref} L_{ref}}{\rho_{ref} {U_{ref}}^2}. \tag{7}$$

However, it needs further calibration by experiments and numerical simulations according to the induced flow field.[21]

2.1.2 Drift-Diffusion model

Notwithstanding the capability of the D-D model in the 3-D body force simulation by Nishida et al.,[26] the model comparison is conducted in 2-D simulations for convenience and simplicity in this study. The electron, the positive ion, and the negative ion are considered with basic plasma chemistry including electron impact ionization, attachment, and recombination. The ionization and attachment coefficients and electron mobility are calculated by BOLSIG+[29] a free electron Boltzmann equation solver, assuming the ambient gas is air (N_2:O_2 = 0.8:0.2).

Here the governing equations to be solved are explained in detail in the previous studies,[9, 24-26, 28, 30] the computational electrohydrodynamic (EHD) force regarded as the two-dimensional body force is expressed as the rate of momentum transfer per unit volume due to collisions,

$$\boldsymbol{f} = e_c(n_p - n_e - n_n)\boldsymbol{E} - \left[\frac{D_p}{\mu_p}\nabla n_p + \frac{D_e}{\mu_e}\nabla n_e + \frac{D_n}{\mu_n}\nabla n_n\right], \tag{8}$$

where n is the plasma density, μ is the charged particle mobility, and their subscript *e, p, n* denote the electron, the positive ion, and the negative ion, D is the coefficients of diffusion. The first term on the right side of Eqn. (8) plays a dominant role and corresponds to the expression used in S-H model in Eqn. (1), while the second term represents the diffusion effect. The obtained 2-D body force in Eqn. (8) is first averaged in phases, then input into the N-S solver for the 2-D simulation of the induced flow, however the spanwise uniformity of body-force distribution is assumed in the 3-D simulation for simplicity.

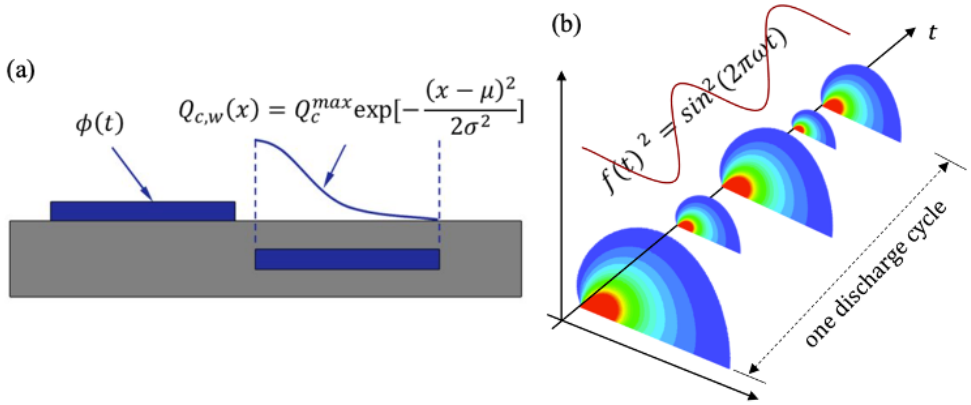

Figure 2. (a) Boundary condition of charged particle in S-H model, following a half Gaussian distribution.[2] (b) Spatial and temporal distribution of body force in S-H model.

2.2 Computational fluid dynamics (CFD)

Two typical flows are considered. First, the flow field is assumed to be globally quiescent and laminar over a flat plate, then the strength of the induced flow is investigated. Second, the body-force models are applied and examined in practical flow control simulations, where the separated flow over a NACA0015 airfoil with a light-stall angle of attack of 12° in turbulence transition state (Reynolds number *is* 63,000) is investigated. The Mach number is 0.2, the specific heat ratio (γ) is 1.4, and the Prandtl number (Pr) is 0.72, those are keeping the same as the previous simulation[16] and the experiment setup.[21] On the surface of the flat plate and the airfoil, no-slip and adiabatic conditions are imposed.

The flow field is described by the 3-D compressible Navier-Stokes equations as below, augmented by the term $\boldsymbol{S}_i$ representing the local forcing on the ionized region by DBD-PA. The non-dimensional forms of the continuity, momentum, energy equations, as well as ideal gas equation are written as follows:

$$\frac{\partial \rho}{\partial t} + \frac{\partial \rho \boldsymbol{u}_k}{\partial x_k} = 0, \tag{9}$$

$$\frac{\partial \rho \boldsymbol{u}_i}{\partial t} + \frac{\partial (\rho \boldsymbol{u}_i \boldsymbol{u}_k + p\boldsymbol{\delta}_{ik})}{\partial \boldsymbol{x}_k} = \frac{1}{Re}\frac{\partial \boldsymbol{\tau}_{ik}}{\partial \boldsymbol{x}_k} + \boldsymbol{S}_i, \tag{10}$$

$$\frac{\partial e}{\partial t} + \frac{\partial ((e+p)\boldsymbol{u}_k)}{\partial \boldsymbol{x}_k} = \frac{1}{Re}\left(\frac{\partial \boldsymbol{u}_l \boldsymbol{\tau}_{kl}}{\partial \boldsymbol{x}_k} - \frac{1}{(\gamma-1)PrM_\infty^2}\frac{\partial \boldsymbol{q}_k}{\partial \boldsymbol{x}_k}\right) + \boldsymbol{S}_k \boldsymbol{u}_k \tag{11}$$

$$p = (\gamma-1)(e - 0.5\rho \boldsymbol{u}_k \boldsymbol{u}_k) \tag{12}$$

where $\boldsymbol{x}_i$ is the position vector, $\boldsymbol{u}_i$ is the velocity vector, $\boldsymbol{q}_k$ is the heat flux vector, ρ is the density, p is the static pressure, e is the total energy per unit volume, $\boldsymbol{\tau}_{ik}$ is the viscous stress tensor, $\boldsymbol{\delta}_{ij}$ is the Kronecker delta, $\boldsymbol{S}_i$ is the body force vector, γ is the ratio of specific heats, t is the time. In S-H model, $\boldsymbol{S}_i$ is directly given by Eqn. (6) with a proper D_c value, while $\boldsymbol{f}_i$ in D-D model (Eqn. (8)) is normalized as

$$\boldsymbol{S}_i = \frac{1}{\rho_\infty U_\infty^2}\boldsymbol{f}_i. \tag{13}$$

2.3 Numerical schemes

To solve the governing equations in Eqn. (9) – (12), this research employs a compressible Navier-Stokes flow solver LANS3D,[31,32] which is extensively used and well validated in recent 30 years. The implicit large-eddy simulations (LES) are conducted for solving the more complex flow field above the airfoil in turbulent transition state.[16] All the spatial derivatives are obtained with a sixth-order

compact difference scheme.[33] Lower-upper symmetric alternating direction implicit and symmetric Gauss-Seidel (ADI-SGS) method is utilized for time integration. 10th order filtering[33] is applied with a filtering coefficient of 0.42.

The current numerical schemes in D-D force computation largely follow Nishida et al.'s previous studies.[9, 26, 30] given by the formula in Eqn. (6). The input time interval of the S-H and the D-D force match the time step of CFD simulation in real scale.

2.4 Computational grids

The information of the computational grid systems for the body force computation and the CFD are listed in Table 1. In the 2-D simulation of the quiescent air, the 2-D computational domains and grids are shown in Fig. 3(a), the D-D force (red zone) is computed and interpolated into the CFD grids (white background). In the 3-D simulations of the separated flow above the airfoil, the C-type grid is designed, the near and far field are shown in Fig. 3(b) and (c), respectively. The spanwise length of the computational region is set to 0.2 times the chord length. The D-D force is interpolated into the actuator zone (highlighted in green). A message passing interface (MPI) between the fluid zones is employed for the parallel computing in CFD simulations.

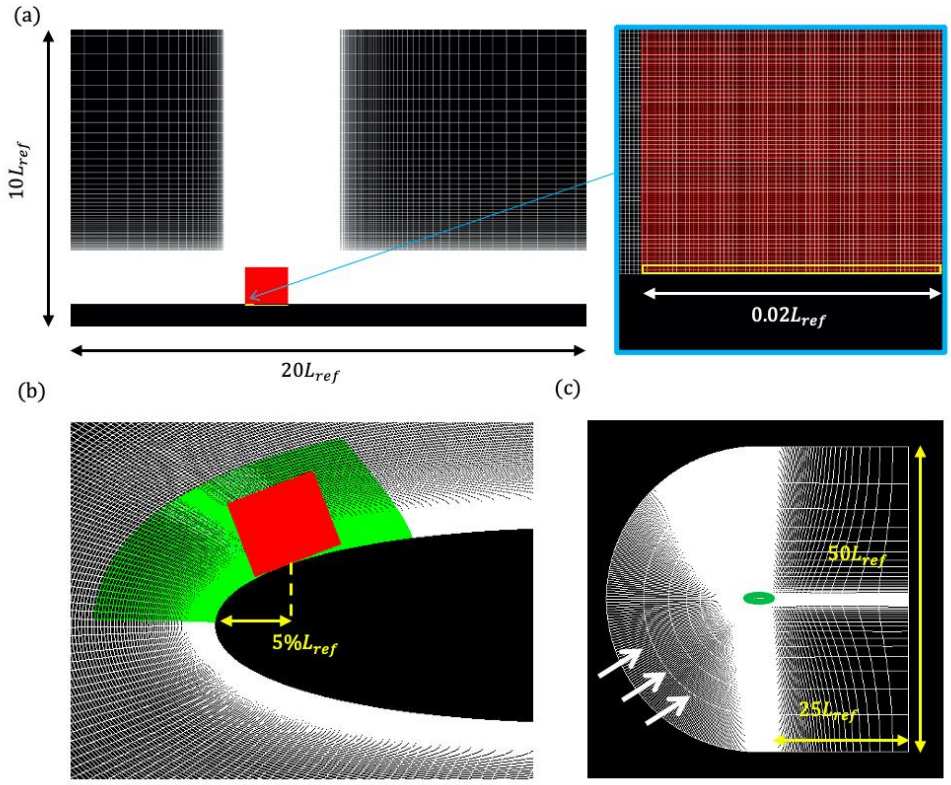

Figure 3. Domain incorporation of the D-D body force (in red) into CFD (in white) for the flat plate (a), and the NACA0015 airfoil (b), the green grids denote the overset actuator zone, the exposed electrode is highlighted in the zoom-in snip; (c) Computational domain of the airfoil and the schematic of inflow, $L_{ref} = c = 0.1\text{m}$.

Table 1. Grid density of the body-force computation and CFD

Computation domain	ξ	η	ζ	Total points
D-D body force (red in Fig. 3a, b)	600	3	250	450,000
Flat plate (white in Fig. 3a)	873	3	416	1,089,504
Airfoil surface (white in Fig. 3b)	759	134	179	18,205,374

Airfoil actuator (green in Fig. 3b)	149	134	111	2,216,226

* In curvilinear coordinates (ξ, η, ζ), ξ and ζ denote wall-parallel and wall-normal directions, respectively, η denotes the spanwise direction in the airfoil case.

2.5 DBD-PA setup

Fig. 4(a) shows the configuration of DBD-PA in the D-D computational domain, which is consistent with Sekimoto et al.'s experiment.[34] The physical parameters as shown in Fig. 4(a) are precalculated in the previous numerical studies using D-D model.[26, 29] The plasma actuator consists of a $160\mu m$ thick Kapton dielectric layer and two $50\mu m$ thick copper electrodes. The thickness of the exposed electrode can be neglected in CFD simulations. A sinusoidal form $0.5\,V_{pp}\sin(2\pi f_{base}t)$ of AC power is applied on the electrodes, the peak-to-peak voltage (V_{pp}) amplitude is from 7kV to 20kV and the base frequency (f_{base}) is set to 10kHz. In the quiescent flow simulation, the continuous mode is applied, therefore the flow is permanently driven by the DBD-PA.

In the separated flow over the airfoil, the exposed electrode of DBD-PA is placed at 5% chord length from the leading edge, the DBD-PA is periodically activated in the duty cycle as shown in Fig. 4(b). It is called burst mode actuation compared to the continuous mode actuation generally used. The burst frequency $f^+ = 500$Hz and the burst ratio $BR = 0.1$. The burst mode with a proper F^+ is well known to have better performance in flow separation control than the continuous mode.[15,16, 19, 22, 34] F^+ and F_{base} are the normalized values of burst and base frequency, respectively.

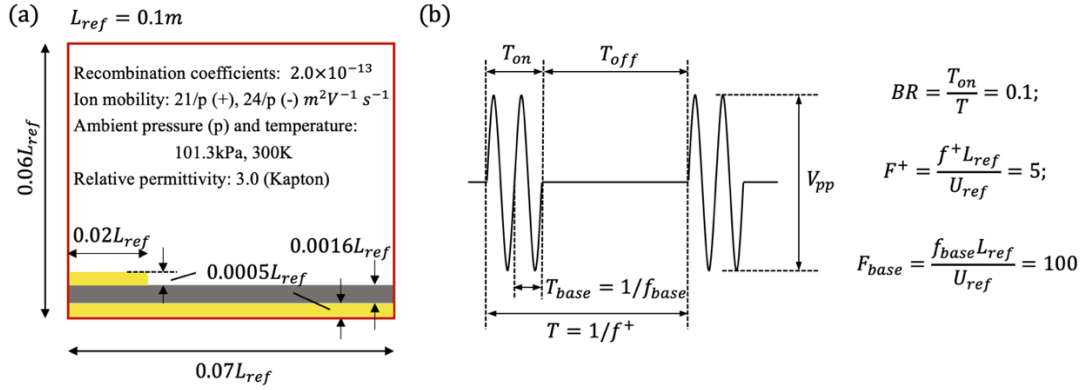

Figure 4. (a) PA configuration and physical parameters in the D-D computation, including electrodes and dielectric layer highlighted in yellow and grey, respectively ($L_{ref} = 0.1m$); (b) Schematic diagram of a bursting wave in burst actuation mode.

2.6 Computational resources

To obtain the time-varying D-D force fields which are necessary as an input data for the flow field simulations, an in-house computation server is used. It takes around 90 hours using one node per case, which computes 4.5 discharge cycles. For the CFD simulations, the supercomputer subsystem named AOBA-A of the Cyberscience Center in Tohoku University is used. 8 nodes are used for computing the flow fields in the divided subdomains with MPI techniques, it takes around 26 hours per case (non-dimensional time $tU_{ref}/L_{ref} = 80$) of the flat-plate flow simulation, and around 70 hours per case (non-dimensional time $tU_\infty/c = 9.6$) of the airfoil flow simulation.

3. Results

3.1 Body force fields of DBD-PA

The body force terms on the right side of Eqn. (10) and (11) are computed by the D-D model and the S-H model. Fig. 5 show the time history of the wall-parallel EHD net force within 3 cycles,

the D-D force computations are conducted at the V_{pp} from 7kV to 20kV. In the case of S-H model, the nondimensional plasma parameter D_c is set to 0.0117 referred to the previous parametric studies,[21] in which the near-field induced flow agrees well with the experiment of $V_{pp} = 7kV$. Due to the lack of strong evidence relating the controlling parameter D_c to the applied voltage, we only plot the results of the S-H model of $D_c = 0.0117$ (SH-Dc0.0117) at the corresponding voltage of 7kV for all the following comparisons.

As shown in Fig. 5 the time variation of body force in S-H model which was developed by Asada et al.[16, 17] assumes to follow the function of $\sin(2\pi F_{base} t)$ in Eqn. (14). The net force is positive all the time and symmetrical between negative- and positive-going phases, that probably overestimates the input power when the body force peak is approximately same with that in the D-D case of 7kV. The time-averaged value of the net body force in Fig. 5(c) are 10.21mN for D-D model at 7kV, 18.45mN for 10kV, 21.07mN for S-H model with $D_c = 0.0117$. The power law of ${V_{pp}}^{1.49}$ agrees with Nishida et al.'s 2-D simulation results[26] in a range of V_{pp} from 10kV to 24kV when the relative permittivity of the dielectric layer (glass epoxy) is set to 5.0.

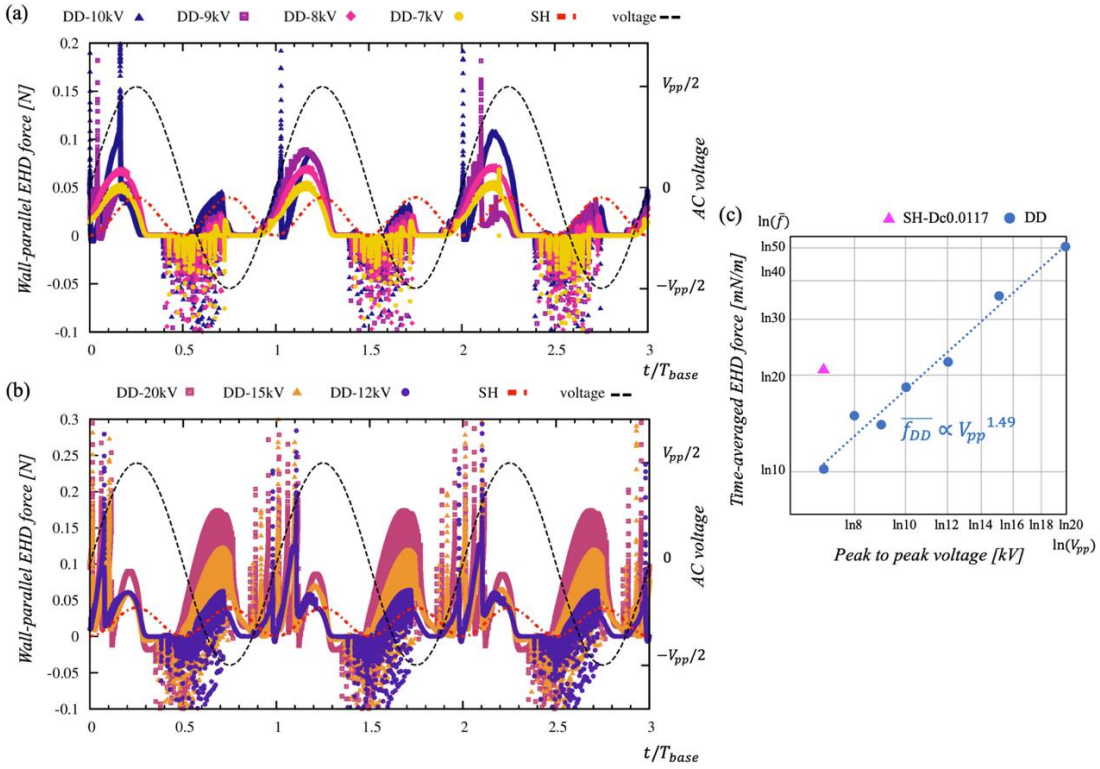

Figure 5. Time history (three periods) of the dimensional EHD net force computed in the entire body-force domain using the D-D model at 7kV, 8kV, 9kV, 10kV (a), and 12kV, 15kV, 20kV (b), as well as the S-H model with $D_c = 0.0117$; (c) Time-averaged D-D body force .vs. peak-to-peak voltage and S-H body force.

3.2 Induced flow in quiescent field

When the body force fields are obtained by D-D or S-H model, it is quite straightforward to relate the force production to the induced flow structure in quiescent air over a flat plate. The time-varying body force terms are incorporated into the right-hand side of the N-S equations, the induced flow fields are then computed by the CFD solver. The time-averaged wall-parallel velocity contours using the D-D model from 7kV to 9kV are compared with the corresponding experimental results,[34]

as well as the S-H model with $D_c = 0.0117$ in Fig. 6(a), which is determined based on the previous study, where Aono et al. conducted showed the guideline of Dc values by the comparison of experimental and computational result with S-H model.[21] Fig. 6(b) shows the maximum velocity measured at 20mm downstream (position A), the far-field numerical and experimental results are compared. The current results are obtained in the flow field averaged from 0.4s to 0.8s.

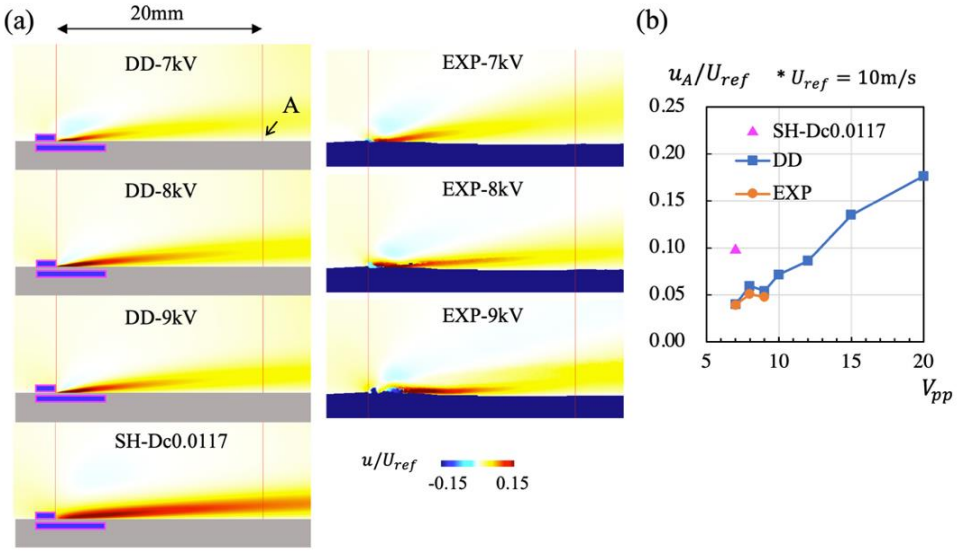

Figure 6. (a) Wall-parallel velocity fields in the present CFD simulations (left) and our previous experiments[34] (right); (b) Far-field velocity (u_A) at 20mm downstream.

The induced flow structures and the downstream velocity (u_A) computed by the D-D model show very good agreement with the experiment. Compared to 8kV, the velocity decline at 9kV is probably caused by the less body force production in Fig. 5(c) due to the unstable EHD force pushing fluid towards downstream in positive-going phase. However, the induced flow of S-H model is much stronger than those of D-D models from 7kV to 9kV, the local velocity at 20mm downstream is even higher than the D-D case of 12kV in Fig. 6(b).

Fig. 7 further shows the near-field velocity profiles in a range of $x/L_{ref} = 0.02$ to 0.08 (2mm to 8mm) in the downstream of the exposed electrode, as shown in the top of Fig. 7(b). The experiment of 9kV shows the remarkable unsteadiness, which is the potential cause of the reversed induced flow at $x/L_{ref} = 0.02$, and the exceeding velocity compared to the D-D result at the other downstream positions. On the other hand, the near-field velocity profiles of the S-H model show the much smaller gradient of the velocity field, compared to the D-D results.

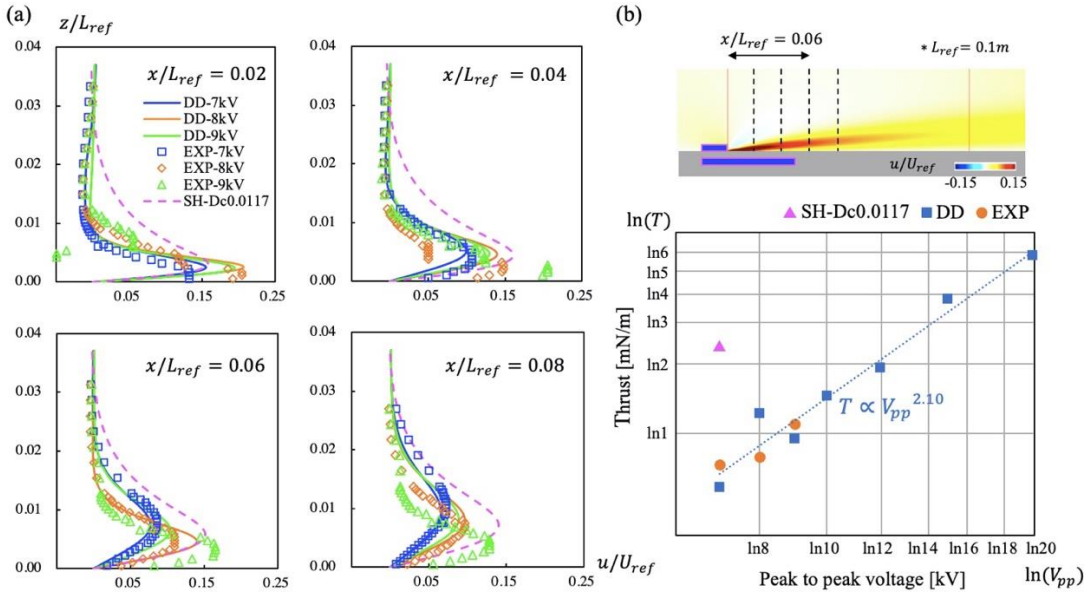

Figure 7. (a) Wall-parallel velocity profiles in the near field; (b) Thrust at 6mm downstream.

3.3 Flow separation control over NACA0015 airfoil

The PA-assisted flow control have gained great interest in a variety of separated flow fields over the Reynolds number from 10^3 to 10^6,[36] and the angle of attack of pre-to-post stall from 10 degrees to 16 degrees. In this report, a comparative study among the D-D model, S-H model and experiment is conducted in the separated flow over a NACA0015 airfoil at a light-stall angle of attack of 12° and a transitional Reynolds number of 63,000. Burst actuation ($F^+ = 5$, $BR = 0.1$) is set to maximize the separation control effect.[35, 37] In the following results, "EXP-7kV" denotes the experimental result with the same setups of flow filed and DBD-PA in Asada et al.'s work,[37] "NOACT" is the case without control.

Fig. 8 shows that the flows are almost completely attached in all the three controlled cases, it also shows little difference between the S-H and the D-D cases either in velocity field or in *TKE* (turbulent kinetic energy) field. The *TKE* has overshoot in the transition position of the shear layer, and the overshoot becomes larger when the transitional shear layer is thick.[36] The chordwise locations of TKE_{max} peaks in Fig. 8(c) show very good agreement with the reattachment positions in Fig. 9(b). However, the S-H case shows the relatively larger *TKE* overshoot compared to the D-D cases, due to the delay of turbulent transition. On the contrary, the early and smooth transition process in the D-D cases results in the smaller *TKE* overshoots.

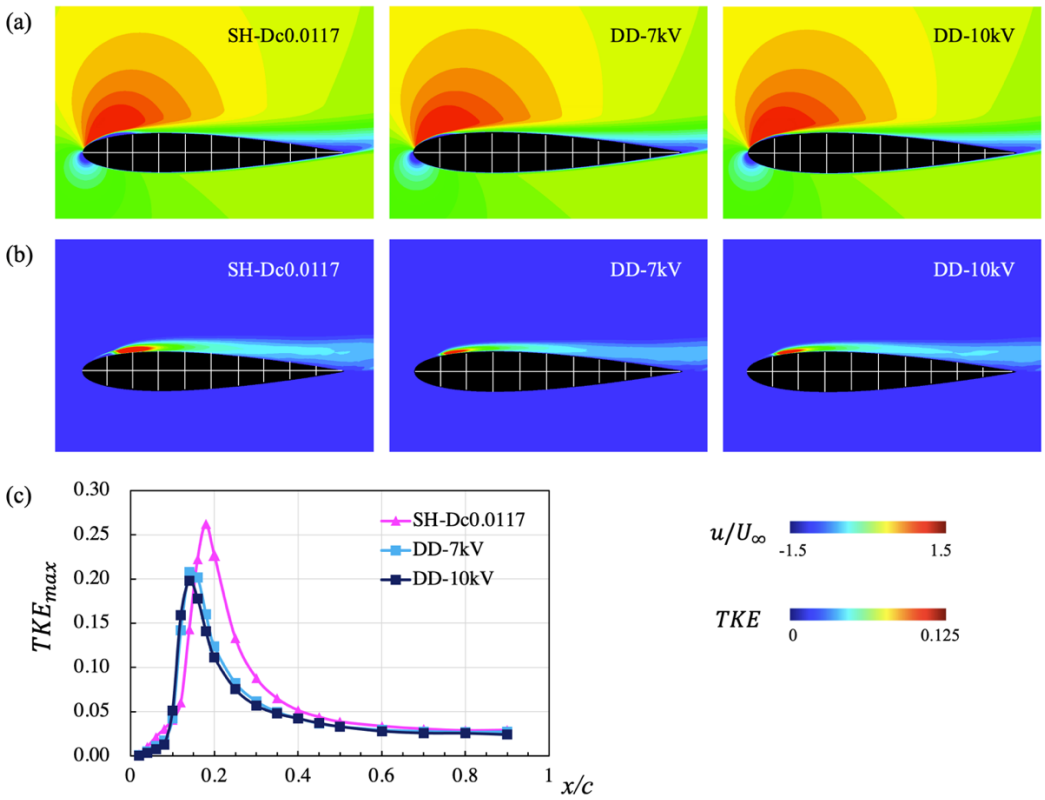

Figure 8. Distribution of chordwise velocity (a), turbulence kinetic energy (b); Spatial development of maximum turbulent kinetic energy (c) obtained from (b).

Distributions of the aerodynamic coefficients in the chordwise direction are further shown in Fig. 9. In the cases with PA control, the time- and span-averaged pressure coefficient (C_p) shows the suction peaks as well as the plateau distributions which corresponds to the so-called laminar separation bubble. The C_p curves indicate the lift increase in the cases with PA control, while the skin-friction coefficient (C_f) shows the reduction of pressure drag, as well as the flow-separated regions shown in the bottom of Fig. 9(b). Better agreement of C_p distribution can be observed between the D-D cases and the experiment at 7kV, compared with the S-H case. As to the C_f curves in Fig. 9(b), it is found that the reattachment points in the D-D cases move closer towards the leading edge compared to the S-H case. The discrepancy of the reattachment position is partly caused by the different location of the maximum induced velocity in the quiescent flow simulation, which is discussed in detail by Chen et al.[28]

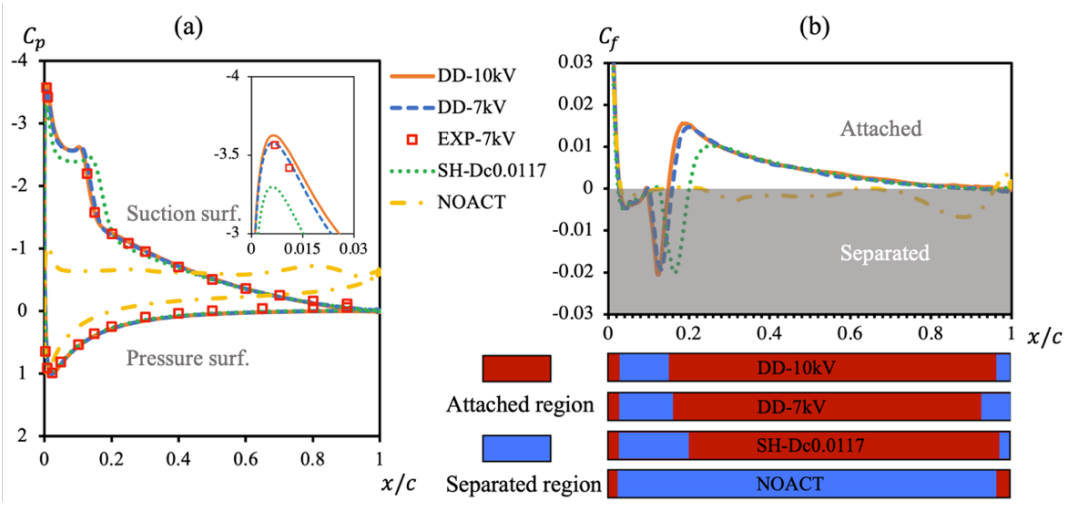

Figure 9. Pressure coefficient (a), skin-friction coefficient (b) along the airfoil chord.

4. Summary and suggestions

In computational studies of PA-assisted flow control, S-H model can be quickly implemented because of the low cost, it has been widely used and also well validated by experiments. On the other hand, D-D model as a high-fidelity body force model has never been employed before in practical flow control simulations. The study shown in Ref. 28 and summarized in this report by the present authors first shows the usage of the two models, as well as the result comparison in the quiescent flow and airfoil flow simulation. Using the different body force model, the effect of separation control is almost the same in the separated airfoil flow, despite the large discrepancy of the induced flow in the quiescent air.

When we consider the cost reduction of the body force computation, for the current flow condition in light separated and turbulent transition state, S-H model is acceptable within the reasonable range of computational accuracy so far as discussions are qualitative. However, it is probably necessary to use the D-D model of high temporal fidelity in fully turbulent flows, as the body-force unsteadiness within the duty cycle may not be neglected.

Acknowledge

The flow field computations presented in this report is performed on the “SX-Aurora TSUBASA” in the Cyberscience Center, Tohoku University. Supports by the center staff are very much acknowledged. This study is also partly supported by the Grants-in-Aid for Scientific Research A (JSPS 18H03816).

References

1 M. Visbal and D. Gaitonde, AIAA paper 2006-3230 (2006).
2 Y. Suzen and G. Huang, AIAA paper 2005-4633 (2005).
3 J.-J. Wang, K.-S. Choi, L.-H. Feng, T.N. Jukes, and R.D. Whalley, Prog. Aerospace Sci. **62**, 52 (2013).
4 S. Sekimoto, T. Nonomura, and K. Fujii, AIAA J. **55**, 1385 (2017).
5 S. Sekimoto, K. Fujii, H. Yoneda, AIAA paper 2020-0825 (2019).
6 E. Peers, X. Huang, and X. Luo, IEEE Trans. Plasma Sci. **37**, 2250 (2009).
7 S. Roy, P. Zhao, A. DasGupta, and J. Soni, AIP Adv. **6**, (2016).

[8] J.P. Boeuf and L.C. Pitchford, J. Appl. Phys. **97**, 103307 (2005).
[9] H. Nishida and T. Abe, J. Appl. Phys. **110**, 013302 (2011).
[10] C.L. Enloe, T.E. McLaughlin, R.D. VanDyken, K.D. Kachner, E.J. Jumper, T.C. Corke, M. Post, and O. Haddad, AIAA J. **42**, 595 (2004).
[11] D.M. Orlov, Modelling and Simulation of Single Dielectric Barrier Discharge Plasma Actuators, Thesis (Ph.D.), University of Notre Dame (2006).
[12] F. Massines, A. Rabehi, P. Decomps, R. Ben Gadri, P. Ségur, and C. Mayoux, J. Appl. Phys. **83**, 2950 (1998).
[13] J.R. Roth, D.M. Sherman, and S.P. Wilkinson, AIAA J. **38**, 1166 (2000).
[14] W. Shyy, B. Jayaraman, and A. Andersson, J. Appl. Phys. **92**, 6434 (2002).
[15] T.C. Corke, C.L. Enloe, and S.P. Wilkinson, Annal Rev. Fluid Mech. **42**, 505 (2009).
[16] K. Asada and K. Fujii, in AIAA *5th Flow Control Conf.* Reston, Virginia (2010), pp. 1–12.
[17] K. Asada, T. Nonomura, H. Aono, M. Sato, K. Okada, and K. Fujii, Int. J. Comp. Fluid Dyn. **29**, 215 (2015).
[18] S. Kawai, T. Bouwhuis, Y. Abe, A. Yakeno, T. Nonomura, H. Aono, A. Oyama, H.W.M.M. Hoeijmakers, and K. Fujii, Theor. Comput. Fluid Dyn. **32**, 805 (2018).
[19] S. Sekimoto, T. Nonomura, and K. Fujii, AIAA J. **55**, 1385 (2017).
[20] M. Kotsonis, S. Ghaemi, L. Veldhuis, and F. Scarano, J. Phys. D. Appl. Phys. **44**, 045204 (2011).
[21] H. Aono, S. Sekimoto, M. Sato, A. Yakeno, T. Nonomura, and K. Fujii, Mech. Eng. J. 2, 15 (2015).
[22] K. Fujii, Appl. Sci. **8**, 546 (2018).
[23] V.I. Gibalov and G.J. Pietsch, J. Phys. D. Appl. Phys. **37**, 2082 (2004).
[24] J.P. Boeuf and L.C. Pitchford, J. Appl. Phys. **97**, 103307 (2005).
[25] A. V Likhanskii, M.N. Shneider, S.O. Macheret, R.B. Miles, A. V Likhanskii, M.N. Shneider, S.O. Macheret, and R.B. Miles, J. Appl. Phys. **103**, 13 (2008).
[26] H. Nishida, T. Nonomura, and T. Abe, AIAA J. **54**, 659 (2016).
[27] D.V. Gaitonde, M.R. Visbal, and S. Rouy, in *Proc. ASME/FEDSM2006* (2006), pp. 1339–1356.
[28] D. Chen, K. Asada, S. Sekimoto, K. Fujii, and H. Nishida, Phys. Fluids 33, 037115 (2021).
[29] URL: http://www.bolsig.laplace.univ-tlse.fr/ for more information about the BOLSIG+ database.
[30] K. Nakai, A. Nakano, and H. Nishida, AIAA J. **1** (2021).
[31] K. Fujii, H. Endo and M. Yasuhara, Activities of computational fluid dynamics in Japan: compressible flow simulations, In High performance computing, 139, John Wiley and Sons Ltd. (1992).
[32] K. Fujii and S. Obayashi, J. Aircraft. **26**, 1123 (1989).
[33] S.K. Lele, J. Comp. Phys. **103**, 16 (1992).
[34] S. Sekimoto, K. Fujii, S. Hosokawa, and H. Akamatsu, Sensors Actuators, A Phys. **306**, 111951 (2020).
[35] H. Aono, S. Kawai, T. Nonomura, M. Sato, K. Fujii, and K. Okada, AIAA J. **55**, 3789 (2017).
[36] M. Sato, K. Okada, K. Asada, H. Aono, T. Nonomura, and K. Fujii, Phys. Fluids **32**, 025102 (2020).
[37] K. Asada, Y. Ninomiya, K. Fujii, and A. Oyama, in *47th AIAA Aerospace. Sci. Meet.* Reston, Virginia, (2009), pp. 1–14.